Nanocolumnar Pt:Ni Alloy Thin Films by High Pressure Sputtering for Oxygen Reduction Reaction

Busra Ergul-Yilmaz[1, z], Zhiwei Yang[2], Assem O. Basurrah[1], Mike L. Perry[2, *], Kimberly S. Reeves[3], David A. Cullen[3], and Tansel Karabacak[4]

[1]Department of Chemistry and [4]Department of Physics & Astronomy, University of Arkansas at Little Rock, Little Rock, Arkansas 72204, USA

[2]Raytheon Technologies Research Center, East Hartford, Connecticut 06108, USA

[3]Center for Nanophase Materials Sciences, Oak Ridge National Laboratory, Oak Ridge, Tennessee 37830, USA

[z]E-mail: bxergul@ualr.edu

Abstract

Self-supported nanocolumnar Pt:Ni thin films (TFs) with varying Pt:Ni atomic ratios and Pt mass loadings were produced on a microporous layer (MPL)-like surface composed of carbon particles by high pressure sputtering and examined as oxygen reduction reaction (ORR) electrocatalysts for polymer electrolyte membrane fuel cells. Cauliflower-like microstructures were observed from scanning electron microscopy imaging. Various Pt:Ni atomic ratios were obtained by simply changing the relative deposition power between Pt and Ni source and investigated by X-ray diffraction and quartz crystal microbalance analysis. Electrochemical characterization of the Pt:Ni-TF/MPL-like-layer/glassy-carbon samples was conducted through benchtop cyclic voltammetry and rotating disk electrode measurements. The electrochemically active surface area (ECSA) was found to be between 22-42 m^2/g for different Pt:Ni atomic ratios. Lower Pt mass loadings exhibited a higher ECSA and the catalytic activity of all Pt:Ni ratios increased with the increase in Pt mass loading. The ORR activity of the Pt:Ni-TFs increased in the order of 3:1 < 1:1 < 1:3 with exhibiting a specific activity of 1781 $\mu A/cm^2$ and mass activity of 0.66 A/mg for the Ni-rich film with 1:3 ratio. The catalytic performance of Pt:Ni-TFs were higher than traditional high surface area carbon supported Pt nanoparticles, elemental Pt nanorods, and Pt-Ni nanorods.

Keywords: Nanocolumnar Pt-Ni thin films, self-supported catalyst, Pt-Ni alloy catalyst, high pressure sputtering (HIPS), oxygen reduction reaction (ORR), polymer electrolyte membrane fuel cell (PEMFC).

Introduction

Successful commercialization of polymer electrolyte membrane fuel cells (PEMFCs) for automotive applications can only be achieved if performance, cost, and durability targets are met.[1] Pt nanoparticles dispersed on high surface area carbon (Pt/C) have been considered the most effective material to catalyze the hydrogen oxidation reaction (HOR) at the anode and oxygen reduction reaction (ORR) at the cathode of a PEMFC. However, limited resources and high cost of Pt are some of the drawbacks of large-scale applications of the fuel cells.[2] In addition, agglomeration of Pt particles and corrosion of

[*] Present address: Largo Clean Energy

carbon support result in lower electrochemical surface area (ECSA) and catalytic efficiency during operation that leads to over-potentials and voltage losses for the ORR.[3]

In order to reduce the amount of expensive Pt and improve catalyst activity toward fuel cell reactions, as well as to improve Pt utilization and stability issues observed in traditional Pt/C electrodes, researchers have considered alloying Pt with transition metals such as Ni, Co, Cu, Fe, Pd, Ir, Ti, V, and Ru electrodes.[1, 4-7] The catalytic properties of a Pt-based material can be tuned by modifying the electronic properties and atomic arrangement.[5, 8, 9] Tuning the structural and electronic properties of transition metals in the core and surface can change the adsorption behavior of oxygen-containing species.[9, 10] Oxygen-containing species decrease the number of surface active sites accessible to molecular oxygen.[11, 12] The addition of a transition metal enhances the ORR activity, which has been attributed to shorter Pt-Pt interatomic distances,[13-15] higher surface roughness due to transitional metal dissolution,[16] changing the d-band vacancy,[17] downshifting the d-band center of Pt,[7, 18] and delayed formation of oxide species.[19] Even though the performance of the ORR catalysts has been improved by alloying with a transition metal, the limited durability of the conventional Pt-based/C electrodes as a result of the corrosion of the Pt, transition metal, and carbon support are remaining.

Nanostructured thin film (NSTF) catalysts, developed by 3M, consist of a continuous polycrystalline Pt and Pt-alloy thin film layer deposited on non-conducting oriented organic pigment (perylene red) whiskers by low pressure sputtering has been shown to address the stability and insufficient ORR activity issues of Pt nanoparticles supported on high surface area carbon.[20-22] They recently reported a mesostructured thin film catalyst with adjustable composition and surface morphology, that was obtained by thermal annealing of a Pt-Ni NSTF catalyst in a reductive atmosphere.[23] The intrinsic catalytic activity of the mesostructured Pt-Ni catalyst was approximately 2 times higher than PtNi-NSTF and 20 times higher than conventional Pt/C catalysts. However, thermal annealing also led the removal of the perylene red from the whiskers, leaving the catalyst unsupported. Moreover, NSTF-based electrodes are susceptible to water accumulation during in-cell operation as they are ~30 times thinner than Pt/C electrodes.[24]

In our earlier work, vertically aligned Pt-Ni nanorods were produced with varying ratios using glancing angle deposition (GLAD),[25-27] which is a self-assembly physical vapor deposition (PVD) technique that involves tilting and rotating the substrate, and investigated as ORR electrocatalysts.[28] The initial specific activity (SA) of the nanorods were 1309 and 907 μA/cm^2 and initial mass activities were ~0.3 and ~0.4 A/mg for 1:1 and 1:3 Pt:Ni ratios, respectively. It was found that Pt-Ni nanorods had higher electrochemically active surface area stability compared to conventional high surface area carbon supported Pt nanoparticles. In order to further enhance the ORR activity, our group recently fabricated vertically aligned Pt-Ni thin films on Ni nanorods (Pt-Ni@Ni-NR) with different Pt-Ni compositions by a combination of GLAD and small angle deposition (SAD)[29-31] techniques and examined them as ORR catalysts in RDE environment.[32] Initial SA and MA values were ~1100 μA/cm^2 and 0.3 A/mg for 3:1, ~2100 μA/cm^2 and 0.5 A/mg for 1:1, and ~3400 μA/cm^2 and 2.0 A/mg for 1:3 Pt:Ni ratios, respectively. Despite the high activities of Pt-Ni@Ni-NR catalysts, they had poor durability, where the catalyst layer was detached from the glassy carbon substrate due to Ni leaching and durability tests could not be performed.

Another continuous layer catalyst approach, to address some of the issues related to catalyst support of Pt nanoparticles and Pt utilization of conventional extended layer approaches, has been the design of self-supported nanocolumnar Pt thin films (Pt-TFs) with controlled morphologies utilizing high pressure sputtering (HIPS)[33-42]. HIPS is a scalable and simple PVD technique to fabricate nanostructured continuous catalyst layers by simply changing the sputtering deposition parameters such as working gas pressure. At high pressures, atoms arrive at the substrate with oblique angles that leads to preferential growth on the islands of higher height due to a shadowing effect and formation of isolated nanocolumnar structures. The growth of columnar geometries can be further enhanced with a rougher underlying substrate so-called microporous-layer-like (MPL-like) surface composed of carbon particles.[42] In our recent work, we studied the fundamental ORR performance of nanocolumnar Pt-TFs deposited on MPL-like surface and found that the MA was increased from 0.06 to 0.26 A/mg when sputtering pressure was increased and Pt mass loading was decreased.[42, 43] In addition, the electrochemically active surface area (ECSA) ranged between 10 to 40 m^2/g as the sputtering pressure was increased and Pt mass loading was decreased.

In this work, we produced a self-supported nanocolumnar Pt:Ni alloy thin film (TF) electrocatalyst with varying Pt to Ni atomic ratios and Pt mass loadings utilizing HIPS and investigated its ORR properties. With this approach, we aimed to enhance the catalyst activity by alloying and eliminate the issues related to corrosion of carbon support in conventional Pt/C by the self-supported catalyst design. HIPS also provides the advantage of being applicable to currently available industrial sputtering systems. Pt:Ni atomic ratios of 3:1, 1:1, and 1:3 were chosen based on the literature data[7, 23, 44, 45] and our previous work.[28, 32, 46] In order to mimic catalyst-coated gas diffusion layers (gas diffusion electrode, GDE) in PEMFCs, Pt:Ni-TFs were deposited on MPL-like surface composed of carbon particles, which better relates the catalyst performance of extended catalyst layers obtained by benchtop tests directly to MEA results.[42]

Experimental

Pt:Ni-TFs were fabricated at 3.93×10^{-2} mbar sputtering pressure by magnetron sputtering (Excel Instruments, India) in a vacuum system. A turbo molecular pump backed by a mechanical pump was used to achieve the base pressure of ~7.0×10^{-7} mbar. The working gas was ultra-high purity argon (Ar, 99.99%). MPL-like surface coated glassy carbon (GC) disk inserts (5 mm OD × 4 mm thick, Pine Instrument) and MPL/GDLs (Sigracet 25) were used as the substrates. The GCs and MPLs were seated on a sample holder that was positioned ~15 cm away from the source (targets) of Pt and Ni (Kurt J. Lesker), which had diameters of ~2.5 cm and ~5.0 cm, respectively. For film uniformity, the sample holder was rotated at a speed of 20 rpm during depositions. For plasma generation, DC power supplies were used. Pt power was set to 40 W and Ni power was set to 40, 80, and 200 W to obtain Pt:Ni-TFs with 1:3, 1:1, 3:1 atomic ratios, respectively. The co-deposition of Pt:Ni-TFs were performed at 45° with respect to the sputter targets (Figure 1). Pt:Ni-TFs with Pt mass loadings of ~20, ~48, and ~94 $\mu g/cm^2$ were fabricated for each atomic ratio. The deposition time of 1:3 ratio was set to 535, 1244, and 2675 s to obtain Pt mass loadings of ~20, ~48, and ~94 $\mu g/cm^2$, respectively. For 1:1 ratio, the deposition time was set to 500, 1274, and 2500 s, and for 3:1 ratio it was set to 553, 1342, and 2684 s to obtain Pt mass loadings of ~20, ~48, and ~94 $\mu g/cm^2$, respectively. The

elemental composition and the mass loading of Pt in the Pt:Ni-TFs were obtained by a quartz crystal microbalance (QCM; Inficon Q-pod QCM monitor; crystal: 6 MHz gold-coated standard quartz). For this measurements, Pt-TFs and Ni-TFs were deposited on QCM crystals at 45° to obtain the desired atomic ratio and Pt mass loading prior to actual alloy fabrications. The Pt loading was determined by comparing the frequencies of the uncoated and the coated crystal. During depositions, a QCM attachment was also facing toward the Ni target to monitor the deposition in situ.

In order to better mimic the morphology of HIPS films in an actual PEMFC, we previously developed a sample preparation method for benchtop electrochemical tests.[42] For this purpose, we produced an MPL-like surface consisting of carbon nanoparticles and treated this surface with oxygen plasma to have a hydrophilic behavior. Details can be found in our previous work. Briefly, 10 µl of carbon ink was drop-cast on GC and allowed to dry overnight at room temperature. Carbon-coated GC was then treated with oxygen (UHP, 99.99%) plasma for 10 s before loading into the sputtering chamber for alloy deposition.

Cyclic voltammetry (CV) and rotating disk electrode (RDE) measurements were performed for electrochemical characterization. For these measurements, a three-electrode glass-cell (Pine Research Instruments) including a hydrogen reference electrode (eDAQ, ET070 Hydroflex), Pt wire counter electrode (Pine Research Instruments), and Pt:Ni-TF/GC disk insert working electrode with 0.196 cm^2 geometric surface area was used. The measurements were carried out at room temperature with a biopotentiostat (WaveDriver 20, Pine Research Instruments) using 0.1 M perchloric acid ($HClO_4$, GFS Chemicals, Inc.; 70% Veritas double distilled) as the working electrolyte. For CV measurements, Pt:Ni-TF/GC disks were cycled between 0.60 V - 1.00 V at a scan rate of 500 mV/s in N_2 saturated (UHP, 99.99%) 0.1 M $HClO_4$ for 50-150 cycles to activate the electrode surface. When the voltammogram reached a steady state, background CVs were collected at 20 mV/s in the potential range of 0.05 V - 1.00 V. Then, the working electrodes were cycled between 0.60 V - 1.00 V at 50 mV/s for 3,000 cycles to test the durability of the catalysts in the acidic environment. ORR activity measurements using RDE was performed at 20 mV/s with 1600 rpm of electrode rotation in oxygen (UHP, 99.99%) saturated 0.1 M $HClO_4$.

Pt:Ni-TFs were deposited on the MPL side of a gas diffusion layer (Sigracet® SGL-25BC) at $3.93x10^{-2}$ mbar sputtering pressure, having Pt mass loadings of ~50 µg/cm^2 and Pt:Ni atomic ratio of 1:3 and 3:1, respectively. The in-cell tests were conducted at the cell temperature of 80°C, with 100% relative humidity of all gases at cell inlets, and 150 kPa abs. of the cell backpressure, in a 12.5 cm^2 (active area) fuel cell fixture by Fuel Cell Technologies Inc., Albuquerque, NM. In this fixture, the cathode and cathode GDL was Pt:Ni-TF coated SGL-25BC. This GDE was pressed against a Nafion®-HP membrane and the other side of the membrane was pre-coated with 0.1 mg_{Pt}/cm^2 of conventional Pt/C catalyst layer which was used as the anode. For the anode GDL, another piece of SGL-25BC was utilized. The conditioning of the cell was performed by scanning the current between 0.1 A/cm^2 and 0.35 V of the cell voltage every 5 min. with increments of 0.1 A/cm^2 for 1 day. H_2//Air and H_2//O_2 with reactant flows resulting in 50% utilization (or 0.05 SLPM as the minimum flow rates) on both sides were used for the conditioning scans. Voltage-current (VI) curve is used to demonstrate electrochemical performance of fuel cells. An electronic load box (Model 890CL, Scribner Associates Inc.) was used to

measure the electrochemical activity, in which the current was scanned up and down from open circuit voltage (OCV) to 0.35 V of the cell voltage with fixed gas flow rates of 0.5 SLPM H_2 and 0.5 SLPM O_2 or 0.5 SLPM Air.

Scanning electron microscopy (SEM, JSM-7000F, JEOL USA) was used for morphological characterization of the Pt:Ni-TFs with different atomic ratios deposited on MPL-like surfaces. The alloy composition and the detailed microstructure of the catalyst layer on MPL (Sigracet 25) were determined by transmission electron microscopy (TEM, Hitachi HF3300, Talos F200X S/TEM). Crystal structure of the Pt:Ni-TFs deposited on MPL-like surfaces was obtained using X-ray diffraction (XRD, Rigaku, Miniflex 600, Cu Kα radiation at 40 kV and 15 mA).

Results and Discussion

Structural Characterization

Top-view SEM images of nanocolumnar Pt:Ni-TFs deposited on MPL-like surfaces with various Pt mass loadings (i.e., film thicknesses) for different Pt:Ni ratios are shown in Figure 2. All of the Pt:Ni-TFs exhibit isolated cauliflower-like structures. Pt:Ni (3:1) TFs feature nanocauliflowers with approximate diameters of ~50 nm, ~75 nm, and ~125 nm for Pt mass loadings of 20, 48, and 94 μg/cm^2, respectively (Figure 2a). The gaps between the columns are ~5 nm for all 3:1 films. Each column is comprised of smaller Pt-Ni branches with approximate diameters of ~4, ~6, and ~13 nm and gaps in between them of a few nanometers for Pt mass loadings of 20, 48, and 94 μg/cm^2, respectively. This columnar microstructure formation is consistent with the morphology of sputtered films deposited at high working gas pressures.[42, 47, 48] Moreover, with the help of the rougher underlying substrate (MPL-like surface), the shadowing effect caused by the higher angular distribution of the atoms impinging on the substrate surface due to enhanced atom collisions at high pressures is further enhanced leading to more columnar nanostructures.[42, 43] As the thickness of the alloy film increases from 20 $\mu g_{Pt}/cm^2$ to 94 $\mu g_{Pt}/cm^2$, the diameter of the nano-cauliflowers and the size of the branches are enhanced due to more material deposited on the substrate surface. Pt:Ni (1:1) TFs, shown in Figure 2b, feature cauliflower-like structures with approximate diameters of ~50 nm, ~115 nm, and ~150 nm, and the gaps of ~4, ~4, and ~9 nm between the columns for Pt mass loadings of 20, 48, and 94 μg/cm^2, respectively. Each column has finer Pt:Ni alloy columns with approximate diameters of ~4, ~8, and ~13 nm and finer gaps of a few nanometers for the Pt mass loadings of 20, 48, and 94 μg/cm^2, respectively.

Similar to the other ratios, Pt:Ni (1:3) films in Figure 2c exhibit cauliflower-like structures with approximate diameters of ~135 nm, ~192 nm, and ~385 nm for the films with Pt mass loadings of 20, 48, and 94 μg/cm^2, respectively. The gaps between the columns are ~4, ~8, and ~12 nm for 20, 48, and 94 μg/cm^2 films, respectively. The finer columns have approximate diameters of ~8 nm and gaps of a few nanometers among them for all the 1:3 films. The diameter of nanocauliflowers for this ratio (1:3) is more than two times higher than the other ratios. 1:3 composition incorporates more Ni atoms that are more mobile and have a higher surface diffusion rate than Pt, leading to large particle/grain/cluster sizes with small particle-particle gaps during thin film deposition.[27]

XRD patterns of nanocolumnar Pt:Ni-TFs with different Pt mass loadings and Pt:Ni ratios deposited on MPL-like surfaces are shown in Figure 3. The 2θ values of monometallic systems of (111) and (200) orientations are 39.76° and 46.24° for Pt and 44.49° and 51.85° for Ni,[28] which are not seen in the XRD profiles indicating the films are alloys of Pt-Ni. The 2θ position of the Pt:Ni films shift to higher angles as the composition of Ni in the alloy is enhanced (40.51° for 3:1, 41.36° for 1:1, and 42.65° for 1:3), indicating smaller distance among the film atoms and smaller lattice constant of the Ni-rich films. The position of 2θ for Pt:Ni (3:1) film is closer to the elemental Pt, which qualitatively shows a Pt rich alloy composition. On the other hand, the 2θ position of 1:3 film is close to the elemental Ni peak, which indicates a Ni-rich alloy film. The d spacing in the thin films were calculated to be ~2.22 Å for Pt:Ni (3:1) films using Bragg's Law ($n\lambda = 2d\sin\theta$), where n is the order of reflection, λ is X-ray wavelength (nm), d is inter-planar spacing of the crystal, and θ is the angle of incidence. The Ni composition of the films were calculated from d spacings using Vegard's Law $d_{PtNi} = Xd_{Pt} + (1 - X)d_{Ni}$ where X is the composition of Pt in the alloy and d_{PtNi}, d_{Pt}, d_{Ni} are the d spacings of the (111) orientations of PtNi, Pt, and Ni. The Ni content in the Pt:Ni (3:1) thin films was calculated to be around ~19 at.%. The difference between the Ni contents of different mass loadings, shown in Table 1, could be a result of the experiment error from deposition to deposition. The Pt:Ni composition obtained from QCM was ~27 at.% Ni for the 3:1 films, which was calculated from the measured mass loadings of individual Pt and Ni depositions with 2.53 and 0.28 μg/cm^2/min deposition rates, respectively, and atomic weight values of 195 for Pt and 59 for Ni. In addition, TEM energy dispersive X-ray spectroscopy indicated a Ni composition of ~27 at.% for 50 $\mu g_{Pt}/cm^2$ mass loading for this ratio. Lower Ni content observed in the XRD results might be due to the existence of non-alloyed Pt in the films aside from measurement errors. However, XRD analysis confirms that Pt is alloyed with Ni and HIPS can be used to alloy Pt and Ni at close-to-room temperature by simply changing the sputter deposition power of Ni. The grain size determination of the alloy films was obtained using Scherrer's formula:

$$D = \frac{0.9\,\lambda}{\beta\cos\theta} \tag{1}$$

where *D* is grain size, *λ* is X-ray wavelength (nm), β is full width half maximum (FWHM), and θ is Bragg angle. The grain size of the Pt:Ni (3:1) TFs ranges from 6 nm to 8 nm with different mass loadings as shown in Table 1, which are close to the Pt:Ni particle/column sizes observed from SEM (~4-13 nm).

The d spacing in the Pt:Ni (1:1) TFs was calculated to be 2.18 Å for all 1:1 films. The Ni contents in the Pt:Ni (1:1) TFs were found to be ~37 at.%, using the Vegard's Law. The Ni composition obtained from QCM was ~51 at.%, which was calculated from the measured mass loadings of individual Pt and Ni depositions with 2.59 and 0.81 μg/cm^2/min deposition rates, respectively. The EDS analysis indicated a Ni composition of ~45 at.% for 50 $\mu g_{Pt}/cm^2$ mass loading. The grain size of the Pt:Ni (1:1) TFs ranged from 6 nm to 9 nm as film thickness was increased (Table 1). The Pt:Ni (1:3) TFs had a d spacing of ~2.11 Å and Ni contents in these films were calculated to be ~67 at.%. The Ni amount obtained from QCM measurement was ~75 at.%, which was calculated from the measured mass loadings of individual Pt and Ni depositions with 2.52 and 2.30

μg/cm^2/min deposition rates, respectively. As mentioned previously, the difference between the XRD and QCM measurements could be due to the experimental errors from deposition to deposition and non-alloyed Pt in the films. The EDS analysis gave a Ni composition of ~75 at.% for 50 $\mu g_{Pt}/cm^2$ mass loading, which is similar to the QCM measurement. The grain size of the Pt:Ni (1:3) TFs increased from 4 nm to 7 nm as the mass loading was increased (Table 1).

The stress in sputtered films is directly related to deposition parameters such as working gas pressure and temperature, which was shown in Thornton's structure zone model.[47, 48] At high working gas pressures, film exhibits a porous and columnar structure of zone 1, which results in tensile strain and is associated with pulling effect and smaller atom-atom distances in thin film literature.[41] Alloying a material also introduces strain as mentioned previously. The apparent strain between the Pt atoms of Pt:Ni-TFs with respect to stress-free bulk Pt was calculated using the d spacing values obtained from Bragg's Law and lattice constant of Pt (3.923 Å)[49] with the formula of $\left({d_{Pt} - d_{PtNi}}/{d_{Pt}} \times 100\right)$. The strain values in the Pt portion of the alloy films were determined to be around 2%, 3%, and 6% for 3:1, 1:1, and 1:3 compositions, respectively, as tabulated in Table 1. The strain value of ~6% for 1:3 composition is higher than the other compositions due to the smaller interatomic distance of ~2.11 Å than others (2.18 Å for 1:1 and 2.22 Å for 3:1). We note that these are not traditional mechanical strain values since one needs to compare measured d spacing of a given material to the spacing of stress-free bulk material of the same kind. Here we aim to estimate the amount of reduction in Pt-Pt atomic spacing of alloy films compared to elemental bulk Pt using strain calculations.

The detailed microstructure of the catalyst layers was analyzed by TEM, in which Pt:Ni-TFs with different Pt:Ni compositions were deposited on MPL as shown in Figure 4. All compositions exhibit a clear columnar structure formation. The nanocolumn size of the 3:1 ratio is ≤8 nm, 1:1 ratio is ≤9 nm, and 1:3 ratio is ≥10 nm. These results are consistent with the XRD data except for 1:3 ratio, which showed larger nanocolumn/grain size from TEM. High-resolution TEM (HRTEM) images in Figure 5 confirm that the cauliflower-like structures are made up of primarily single-crystal Pt:Ni columnar grains with diameters ~10 nm and lengths ~20 nm. The insets in Figure 5 are fast Fourier transform (FFT) patterns calculated from the corresponding red box in each image. The single set of diffraction spots correspond to the lattice planes visible in each image; (111) planes in the case of (3:1) and (1:3) and (002) planes in the case of (1:1). This provides further evidence that the shadowing effect can enhance the formation of single-crystal columnar structures even at room temperature conditions.[28] The catalyst layer thickness was ~45 nm for 3:1, while it was ~100 nm for 1:3 film, which is expected due to higher Ni amount in the alloy of a similar Pt mass loading. Alloy formation at low temperatures during HIPS could be due to the preferential growth of crystalline phases with low adatom mobilities promoted by the shadowing effect.[50]

Electrochemical Characterization

Fig. S1 shows the CVs of nanocolumnar Pt:Ni (3:1) TFs with different Pt mass loadings deposited on MPL-like surfaces before and after 3,000 cycles of durability testing that

involved potential cycling between 0.60 V – 1.00 V in 0.1 M $HClO_4$. The CVs show characteristic regions of a pure Pt surface with hydrogen adsorption and desorption peaks between 0.05 V – 0.40 V, double layer capacitive current regime between 0.40 V – 0.60 V, and Pt oxidation and reduction peaks between 0.70 V – 1.00 V.[51, 52] H underpotential deposition region below 0.40 V exhibits Pt-like features agreeing with the literature, in which the peaks around 0.11 V are assigned to Pt (110) and the ones around 0.30 V correspond to Pt (100) orientations. The ECSA of the Pt:Ni-TFs was calculated by integrating the charge in the hydrogen adsorption region (0.05 V – 0.40 V) of the CVs, after subtracting the double layer charge from the total current using the following equation to convert the measured charge to ECSA:[51]

$$ECSA_{Pt,cat}(m^2 g_{Pt}^{-1}) = \left[\frac{Q_{H-adsorption}\ (\mathrm{C})}{210\ (\mu\mathrm{C\ cm_{Pt}^{-2}})\ L_{Pt}\ (\mathrm{mg_{Pt}\ cm^{-2}})\ A_g\ (\mathrm{cm^2})}\right] \times 10^5 \quad (2)$$

where $Q_{H\ adsorption}$ of 210 μC cm^{-2} is the charge of full coverage of H for clean polycrystalline Pt, A_g (cm^2) is the geometric surface area of the glassy carbon electrode (0.196 cm^2), and L_{Pt} is the Pt loading (mg_{Pt} cm^{-2}) of the working electrode. The initial ECSAs were determined to be 35, 28, and 22 m^2/g for Pt:Ni (3:1) TFs with Pt mass loadings of 20, 48, and 94 $\mu g_{Pt}/cm^2$, respectively. Higher ECSA at lower loadings could be due to better penetration of the electrolyte through the catalyst layer because of the smaller diameters (~50 nm) of nanocauliflowers of a thin catalyst layer at low mass loadings compared to the larger column diameters (~125 nm) of higher loading and thicker Pt:Ni-TF as observed by SEM. The ECSA loss after durability cycling was found to be 26%, 21%, and 32% for the films with Pt mass loadings of 20, 48, and 94 $\mu g_{Pt}/cm^2$, respectively.

The electrocatalytic performance of Pt:Ni thin film electrocatalysts is reported as their area-specific (SA; current produced per active surface area) and mass-specific (MA; current produced per Pt mass loading) activities using the ORR kinetic current obtained from the CVs and using the mass-transport correction for RDE measurements:[51]

$$i_k = {(i_{lim} \times i)}/{(i_{lim} - i)} \quad (3)$$

where i_k is the kinetic current, i_{lim} is the measured limiting current, and i is the measured current at a specific potential (0.90 V). The measured current at 0.9 V should be between $0.1 i_{lim} < i < 0.8 i_{lim}$ for Eq. 3 to be valid.[53] Fig. S2 shows the ORR polarization curves of Pt:Ni (3:1) TFs with different Pt mass loadings deposited on MPL-like surfaces before and after durability cycling. The mixed kinetic-diffusion controlled region is observed between 0.80 V – 1.00 V and diffusion-limited current region is between 0.40 V – 0.80 V in these ORR polarization curves. The diffusion-limited currents for all electrodes were normalized to the GC disk area and are similar or close to the theoretical value of 5.7 mA/cm^2 at room temperature for 1600 rpm rotation speed.[19] Table 2 shows the SA and MA values, which were determined using Eq. 3. The SA increases from 586 to 955 $\mu A/cm^2$ as the Pt mass loading in the film is increased from 20 $\mu g_{Pt}/cm^2$ to 94 $\mu g_{Pt}/cm^2$, which could be due to slightly bigger grain/particle size of Pt-Ni alloy nanostructures (~8 nm) for 94 $\mu g_{Pt}/cm^2$ compared to 20 $\mu g_{Pt}/cm^2$ (~6 nm) observed by XRD. The MA value of ~0.20 A/mg is similar for all loading values of 3:1 films, which indicates poor Pt utilization for this alloy ratio. The MA could be enhanced by shortening

the interatomic distance by a strained lattice, which will be discussed later in the paper. The SA loss after durability cycling is between 1–16%, while the MA loss ranges from 25% to 43%.

Fig. S3 shows the voltammograms of nanocolumnar Pt:Ni (1:1) TFs with Pt mass loadings of 20, 48, and 94 $\mu g_{Pt}/cm^2$ deposited on MPL-like surfaces before and after durability cycling. The underpotentially deposited hydrogen (H_{upd}) region between 0.05 V – 0.4 V exhibits broad features for the 1:1 films of different Pt loadings, indicating that lower coordinated Pt atoms are on the surface and crystalline facets are small.[54] Using Eq. 2, the ECSA was determined to be 34, 27, and 26 m^2/g for Pt:Ni (1:1) TFs with Pt mass loadings of 20, 48, and 94 $\mu g_{Pt}/cm^2$, respectively. Higher ECSA values observed at lower loadings, similar to the 3:1 ratio, are believed to be due to the smaller cauliflower diameters of ~50 nm opposed to ~150 nm of higher loadings. The ECSA loss after durability testing was calculated to be 26%, 22%, and 23% for the Pt:Ni (1:1) films with Pt mass loadings of 20, 48, and 94 $\mu g_{Pt}/cm^2$, respectively.

The ORR polarization curves of Pt:Ni (1:1) TFs with different film thicknesses are shown in Fig. S4. The SA and MA values were calculated using Eq. 3, which are listed in Table 2. The initial SA ranges from 1095 $\mu A/cm^2$ to 1654 $\mu A/cm^2$ as the Pt mass loading increases from 20 $\mu g_{Pt}/cm^2$ to 94 $\mu g_{Pt}/cm^2$, which might be due to the grain/column size enhancement of the Pt:Ni (~4 to ~13 nm) as observed by SEM. The MA is between 0.33 – 0.43 A/mg that is about ~2 times higher than 3:1 ratio (~0.20 A/mg) that is consistent with ~1.7 times enhancement in SA of the 1:1 alloy film compared to that of 3:1 and might also indicate a better utilization of the Pt for this composition due to change in film microstructure. The SA loss after durability cycling is between ~27 – 46%, while the MA loss is between ~46 – 60%. This shows that the stability of the 1:1 catalyst is not as good as 3:1 film. Overall, the ORR activity of 1:1 ratio is ~2 times higher than 3:1 ratio while 3:1 ratio has a better stability.

The CVs of Pt:Ni (1:3) TFs deposited on MPL-like surfaces with different Pt mass loadings before and after durability cycling are shown in Fig. S5. The H_{upd} region between 0.05 V – 0.4 V exhibits broad features for the all 1:3 films, indicating that lower coordinated Pt atoms are on the surface and crystalline facets are small.[54] The ECSA values were calculated using Eq. 2 and found to be 42, 38, and 34 m^2/g for Pt:Ni (1:3) TFs with Pt mass loadings of 20, 48, and 94 $\mu g_{Pt}/cm^2$, respectively. As also observed for the other compositions, lower loadings exhibit higher ECSAs likely due to smaller nanocauliflower diameters. The ECSA loss after durability cycling is 21%, 32%, and 38% for the films with Pt mass loadings of 20, 48, and 94 $\mu g_{Pt}/cm^2$, respectively.

The ORR polarization curves of Pt:Ni (1:3) TFs with different thicknesses are shown in Fig. S6. The SA and MA values were derived from these curves using Eq. 3. As can be seen from Table 2, the SA increases from 1196 $\mu A/cm^2$ to 1842 $\mu A/cm^2$ as the Pt loading is increased from 20 $\mu g_{Pt}/cm^2$ to 94 $\mu g_{Pt}/cm^2$. This could be due to the smaller grain size of 20 $\mu g_{Pt}/cm^2$ film (~4 nm) compared to 94 $\mu g_{Pt}/cm^2$ film (~7 nm) as observed by XRD analysis. The SA of 48 $\mu g_{Pt}/cm^2$ is quite similar to 94 $\mu g_{Pt}/cm^2$ likely due to their similar grain sizes (~7 nm). The MA ranges from 0.51 to 0.66 A/mg, indicating an efficient utilization of Pt. However, the loss in MA due to durability cycling is quite high, which is

between ~47-70%. This could be due to higher Ni-leaching in this Ni-rich film that might take away Pt atoms along with it. The SA loss is between ~32-52%.

Overall, it was found that the ORR activity of nanocolumnar Pt:Ni-TFs increases with the increase in Ni content in the following order: 3:1 < 1:1 < 1:3. We selected the Pt loading of 48 $\mu g_{Pt}/cm^2$ from all compositions to compare their electrochemical and in-cell behaviors. The CVs and ORR polarization curves of Pt:Ni-TFs with different atomic ratios are shown in Figure 6. The 1:3 and 1:1 alloy compositions exhibit similar initial CVs in Figure 6a, while 3:1 has more Pt-like features with more distinctive and sharper (110) and (100) peaks. Meanwhile, the voltammograms after durability cycling evolve to more Pt-like features for all compositions. The capacity of the double layer is independent of the H_{upd} region (electrochemically active surface area).[54] The initial ECSAs were calculated to be 28, 27, and 38 m^2/g for the compositions of 3:1, 1:1, and 1:3, respectively. Higher ECSA of 1:3 ratio could be due to atomic roughening as a result of partially leaching of Ni by the acidic electrolyte, and the more Ni content leads to larger particle size giving more surface area (since Pt loading is the same),[28] while on the other hand, such roughening is expected to be less as the Ni amount is reduced as in the case of 3:1 and 1:1 alloy films. Hydrophilicity of Pt:Ni-TFs were similar for all of Pt:Ni ratios with a contact angle of ~20°, therefore it should not introduce any significant differences in the penetration of electrolyte and on ECSA. The ECSA loss after durability cycling is 21%, 22%, and 32% for the 3:1, 1:1, and 1:3 ratios, respectively. Higher ECSA loss of the 1:3 film might be attributed to more Ni leaching at this ratio. The ORR performance of the catalysts was determined from the polarization curves in Figure 6c-d. The SA was calculated to be 710, 1183, and 1781 $\mu A/cm^2$ for the compositions of 3:1, 1:1, and 1:3, respectively. The 1:3 composition has the highest intrinsic catalytic activity compared to other compositions, which might be due to smaller interatomic distance and slightly larger crystal grain size (~7 nm) of this composition. The SA loss after durability cycling was about ~1%, 33%, and 52% for the 3:1, 1:1, and 1:3 films, respectively. The MA values were 0.20, 0.33, and 0.66 A/mg for the films with the 3:1, 1:1, and 1:3 atomic ratios, respectively. The enhancement in MA can be attributed to the increase in intrinsic activity of the films and higher number of available Pt surface sites per geometric area of the catalyst due to roughened surface because of more Ni leaching compared to lower Ni compositions. However, the MA loss after durability cycling was 67% for the 1:3 film, while it was 20% and 52% for the 3:1 and 1:1 films. Prior to durability cycling, the surface of 3:1 ratio is already Pt dominated and only small amount of Ni available for leaching out, therefore additional cycles did not have a notable effect in the activity for 3:1 ratio. On the other hand, the surface of 1:3 ratio is Ni dominated, while 1:1 is between 3:1 and 1:3, and a large amount of Ni available for leaching out, therefore, durability cycling may result in significant Ni leaching which could cause a decrease in their ORR activity as also observed by enhanced SA loss of these higher Ni content ratios.[55, 56] In addition, significant Ni leaching may generate core-shell structure. After the potential cycles, all 3 samples may result in similar Pt-rich shell, therefore having similar MA and SA.

The catalytic performance of nanocolumnar Pt:Ni-TFs with varying compositions and Pt mass loadings was summarized in Table 2. It can be clearly seen that the 1:3 atomic ratio gives the highest activity compared to the 3:1 and 1:1 ratios. This activity enhancement could be attributed to the higher apparent strain values (~6%) which results in shorter

interatomic distances[13-15] and higher surface roughness due to transitional metal dissolution[16] (dealloying/leaching of Ni) that increases the number of surface Pt sites. The MA of 0.66 A/mg for 1:3 ratio is ~1.5 times higher than GLAD Pt-Ni nanorods[28] and 5 times higher than GLAD Pt nanorods[57]. The Pt:Ni (1:3) TF also exhibit higher activities than conventional Pt/C catalysts (MA: ~0.21-0.51 A/mg, SA: ~265-602 μA/cm^2) in RDE environment.[58] The SA of Pt:Ni (1:3) TF (1781 μA/cm^2) is higher than Pt/C and higher or similar to polycrystalline Pt (~800-2500 μA/cm^2).[58]

In our recent elemental Pt work, we found that Pt films produced at high sputtering pressure formed nanocauliflower-like structures and had higher electrochemical activity compared to the films produced at low sputtering pressure.[42] Therefore, the sputtering pressure was set to a high value for this Pt:Ni alloy work. However, in addition to HIPS films, we also fabricated a more conventional Pt:Ni-TF at low sputtering pressure to investigate if there would be a notable change on the morphology and electrochemical activity that is different than what was observed in HIPS alloy films. For this purpose, the alloy ratio that gave the highest activity among HIPS alloy films was selected, which was 1:3 ratio with ~50 μg$_{Pt}$/cm^2 mass loading. Working gas pressure was set to 3.73x10^{-3} mbar and deposition time was 1154 s. Top-view SEM image of Pt:Ni (1:3) TF with ~50 μg$_{Pt}$/cm^2 deposited at low sputtering pressure is shown in Fig. S7. Denser and packed nanocolumnar structures were observed compared to those of HIPS films. The bundle of nanocolumnar structures had an approximate diameter of ~120 nm with ~10 nm individual columns, which was slightly larger than ~8 nm nanocolumns of the 1:3 HIPS film. Denser microstructure is consistent with reduced shadowing effect at low sputter pressure conditions. However, column structure is still present in the low pressure film and is believed to originate from a limited shadowing effect due to the 45° tilt angle of the substrate holder with respect to Pt and Ni targets as illustrated in Figure 1.

Fig. S8 shows the XRD profile of conventional Pt:Ni (1:3) TF deposited at low sputtering pressure. The (111) peak of 1:3 film is around 42.94° which is consistent with the peak position of 1:3 HIPS film (42.65°). The d spacing in the film was calculated to be 2.11 Å that is similar to the 1:3 HIPS film (2.12 Å). Ni content in the (1:3) film deposited at low sputtering pressure was 70 at.%, as determined by Vegard's Law, which is close to the HIPS film with a similar mass loading (64 at.%). The grain size was determined to be ~9 nm using Eq. 1, which is slightly larger than the 1:3 HIPS film (~7 nm). The apparent strain on the Pt atoms of the alloy film was determined from d spacing and found to be 7%, which is also similar to the 1:3 HIPS film (6%) due to the similar interatomic distance of ~2.11 Å.

The CVs and ORR polarization curves of 1:3 film deposited at low sputtering pressure before and after 3,000 cycles of durability tests are shown in Fig. S9. ECSA was calculated to be 28 m^2/g, using Eq. 2, which is 26% lower than the 1:3 HIPS film with a similar mass loading. Observing a lower ECSA could be due to less shadowing effect and columnar structure formation at low pressure conditions. The ECSA loss after durability cycling was 39%, which is higher than the HIPS film with 32% loss. SA of 568 μA/cm^2 and MA of 0.16 A/mg were calculated from polarization curves using Eq. 3, which are more than 3 times lower than the 1:3 HIPS film. The SA and MA loss after durability cycling were 14% and 50%, respectively. These results indicate that the dense and packed morphology of the nanocolumnar structures at low pressure results in a decrease

in the electrochemical activity because it might be preventing the penetration of the electrolyte through the catalyst layer. This observation further confirms that there is a need for high pressure so that the columnar morphology can be improved, and electrochemical activity can be enhanced.

In addition, we performed preliminary MEA tests to compare the in-cell activity of the Pt-rich and Ni-rich HIPS alloy films of Pt:Ni (3:1) and Pt:Ni (1:3) with Pt mass loading of 48 $\mu g_{Pt}/cm^2$. These films were deposited on an MPL/GDL and pressed with a half MEA consisting of a non-catalyzed GDL and a membrane with traditional Pt/C catalyst on one side to build into a PEMFC. Oxygen transport issues were observed for both alloy films due to non-sufficient catalyst porosity. Ni composition after the in-cell testing was found to be ~25 at.% for 3:1 and ~33 at.% for 1:3 by EDS analysis, which indicates that after potential cycles Ni leaches significantly and this may result in a similar Pt-rich shell for both ratios. In-cell test results did not differ significantly for different Pt:Ni ratios (Fig. S10). Therefore, true catalyst activity is believed to be hindered by the mass transport issues in the catalyst layers. Ni has a high surface diffusion rate that leads to large particle/grain/cluster sizes with small column-column gaps during thin film deposition, which can result in poor mass transport in MEA tests. To overcome the oxygen mass transport issues with this design, nanocolumnar Pt:Ni thin films can be supported on carbon particles. While nanocolumnar microstructure can provide a sufficient surface-to-volume ratio for efficient Pt utilization, the conformal Pt:Ni shell with larger crystal grain sizes covering the carbon support surface can eliminate the durability issues associated with catalyst dissolution, agglomeration, and carbon corrosion, which will be studied in future work.

Conclusion

Self-supported nanocolumnar/cauliflower-like Pt:Ni-TFs with varying compositions and Pt mass loadings were fabricated on MPL-like surfaces by high pressure sputtering and investigated as ORR electrocatalysts. The alloy compositions of 3:1, 1:1, and 1:3 films were obtained by simply changing the power of the sputter deposition and the atomic ratio was determined by XRD, QCM and TEM analysis. Tuning the strain of atoms on the catalyst surface by alloying Pt with Ni reduced the amount of Pt used and enhanced the ORR activity due to the expected activity-enhancing electronic structure and arrangements of surface atoms in the near-surface region. Overall, the ORR activity of all compositions increased as the Pt mass loading was increased consistent with the observed increase in crystal grain size with mass loading. For a set mass loading, catalytic performance of the Pt:Ni-TFs increased in the order of 3:1 < 1:1 < 1:3 with the 1:3 films exhibiting an activity of 1781 $\mu A/cm^2$ and 0.66 A/mg for 48 $\mu g_{Pt}/cm^2$ mass loading. The ECSA was 38 m^2/g for this electrode, while 32% of it was lost after durability cycling. Overall, the electrocatalytic performance of the Pt:Ni-TFs in RDE environment are better than traditional Pt/C catalysts, HIPS Pt thin films, GLAD Pt nanorods, and GLAD Pt-Ni nanorods. The ORR activity can be further enhanced by thermal treatment (annealing) and depositing these nanocolumnar alloy nanostructures onto carbon powder, which will be investigated in future work.

Acknowledgements

This material is based upon work supported by the U.S. Department of Energy's Office of Energy Efficiency and Renewable Energy (EERE) under the Fuel Cell R&D Award Number DE- EE0007652, Project ID FC157. Electron microscopy was conducted at the Center for Nanophase Materials Sciences, which is a DOE Office of Science User Facility. The Talos F200X S/TEM tool provided by US DOE, Office of Nuclear Energy, Fuel Cycle R&D Program, and the Nuclear Science User Facilities. The UA Little Rock authors thank the UALR Center for Integrative Nanotechnology Sciences for helping with SEM imaging.

Disclaimer

References

1. D. Banham and S. Ye, Current status and future development of catalyst materials and catalyst layers for proton exchange membrane fuel cells: an industrial perspective. *ACS Energy Lett.,* **2** (3), 629-638 (2017).
2. H. Lv, D. Li, D. Strmcnik, A. P. Paulikas, N. M. Markovic, and V. R. Stamenkovic, Recent advances in the design of tailored nanomaterials for efficient oxygen reduction reaction. *Nano Energy,* **29**, 149-165 (2016).
3. S. Shrestha, Y. Liu, and W. E. Mustain, Electrocatalytic activity and stability of Pt clusters on state-of-the-art supports: a review. *Catal. Rev.,* **53** (3), 256-336 (2011).
4. S. Kühl and P. Strasser, Oxygen electrocatalysis on dealloyed Pt nanocatalysts. *Top. Catal.,* **59** (17), 1628-1637 (2016).
5. M. Shao, Q. Chang, J.-P. Dodelet, and R. Chenitz, Recent advances in electrocatalysts for oxygen reduction reaction. *Chem. Rev.*, **116** (6), 3594-3657 (2016).
6. A. Kongkanand and M. F. Mathias, The priority and challenge of high-power performance of low-platinum proton-exchange membrane fuel cells. *J. Phys. Chem. Lett.,* **7** (7), 1127-1137 (2016).
7. V. R. Stamenkovic, B. S. Mun, M. Arenz, K. J. Mayrhofer, C. A. Lucas, G. Wang, P. N. Ross, and N. M. Markovic, Trends in electrocatalysis on extended and nanoscale Pt-bimetallic alloy surfaces. *Nat. Mater.,* **2007,** *6* (3), 241-247.
8. F. Maroun, F. Ozanam, O. Magnussen, and R. Behm, The role of atomic ensembles in the reactivity of bimetallic electrocatalysts. *Science*, **293** (5536), 1811-1814 (2001).
9. L. Gan, M. Heggen, S. Rudi, and P. Strasser, Core–shell compositional fine structures of dealloyed Pt x Ni1–x nanoparticles and their impact on oxygen reduction catalysis. *Nano Lett.,* **12** (10), 5423-5430 (2012).

10. O. T. Holton and J. W. Stevenson, The role of platinum in proton exchange membrane fuel cells. *Plat. Met. Rev.,* **57** (4), 259-271 (2013).
11. P. Strasser, S. Koh, T. Anniyev, J. Greeley, K. More, C. Yu, Z. Liu, S. Kaya, D. Nordlund, and H. Ogasawara, Lattice-strain control of the activity in dealloyed core–shell fuel cell catalysts. *Nature Chem.,* **2** (6), 454-460 (2010).
12. C. Wang, N. M. Markovic, and V. R. Stamenkovic, Advanced platinum alloy electrocatalysts for the oxygen reduction reaction. *ACS Catal.,* **2** (5), 891-898 (2012).
13. Q. Jia, W. Liang, M. K. Bates, P. Mani, W. Lee, and S. Mukerjee, Activity descriptor identification for oxygen reduction on platinum-based bimetallic nanoparticles: in situ observation of the linear composition–strain–activity relationship. *ACS Nano,* **9** (1), 387-400 (2015).
14. I. E. Stephens, A. S. Bondarenko, U. Grønbjerg, J. Rossmeisl, and I. Chorkendorff, Understanding the electrocatalysis of oxygen reduction on platinum and its alloys. *Energy Environ. Sci.,* **5** (5), 6744-6762 (2012).
15. C. Wang, M. Chi, D. Li, D. Strmcnik, D. Van der Vliet, G. Wang, V. Komanicky, K.-C. Chang, A. P. Paulikas, and D. Tripkovic, Design and synthesis of bimetallic electrocatalyst with multilayered Pt-skin surfaces. *J. Am. Chem. Soc.,* **133** (36), 14396-14403 (2011).
16. T.-Y. Jeon, S. J. Yoo, Y.-H. Cho, K.-S. Lee, S. H. Kang, and Y.-E. Sung, Influence of oxide on the oxygen reduction reaction of carbon-supported Pt− Ni alloy nanoparticles. *J. Phys. Chem. C,* **113** (45), 19732-19739 (2009).
17. S. J. Hwang, S.-K. Kim, J.-G. Lee, S.-C. Lee, J. H. Jang, P. Kim, T.-H. Lim, Y.-E. Sung, and S. J. Yoo, Role of electronic perturbation in stability and activity of Pt-based alloy nanocatalysts for oxygen reduction. *J. Am. Chem. Soc.,* **134** (48), 19508-19511 (2012).
18. J. Rodriguez, Physical and chemical properties of bimetallic surfaces. *Surf. Sci. Rep.,* **24** (7-8), 223-287 (1996).
19. K. Mayrhofer, D. Strmcnik, B. Blizanac, V. Stamenkovic, M. Arenz, and N. Markovic, Measurement of oxygen reduction activities via the rotating disc electrode method: From Pt model surfaces to carbon-supported high surface area catalysts. *Electrochim. Acta,* **53** (7), 3181-3188 (2008).
20. M. K. Debe, Tutorial on the fundamental characteristics and practical properties of nanostructured thin film (NSTF) catalysts. *J. Electrochem. Soc.,* **160** (6), F522 (2013).
21. M. Debe, Novel catalysts, catalysts support and catalysts coated membrane methods. *Handbook of fuel cells* (2010).
22. M. K. Debe, R. T. Atanasoski, and A. J. Steinbach, Nanostructured thin film electrocatalysts-current status and future potential. *ECS Trans.,* **41** (1), 937 (2011).
23. D. F. Van Der Vliet, C. Wang, D. Tripkovic, D. Strmcnik, X. F. Zhang, M. K. Debe, R. T. Atanasoski, N. M. Markovic, and V. R. Stamenkovic, Mesostructured thin films as electrocatalysts with tunable composition and surface morphology. *Nat. Mater.,* **11** (12), 1051-1058 (2012).
24. F. T. Wagner, B. Lakshmanan, and M. F. Mathias, Electrochemistry and the future of the automobile. *J. Phys. Chem. Lett.,* **1** (14), 2204-2219 (2010).
25. A. Barranco, A. Borras, A. R. Gonzalez-Elipe, and A. Palmero, Perspectives on oblique angle deposition of thin films: From fundamentals to devices. *Prog. Mater. Sci.,* **76**, 59-153 (2016).

26. Y. He and Y. Zhao, Advanced multi-component nanostructures designed by dynamic shadowing growth. *Nanoscale,* **3** (6), 2361-2375 (2011).
27. T. Karabacak, Thin-film growth dynamics with shadowing and re-emission effects. *Journal of Nanophotonics,* **5** (1), 052501 (2011).
28. N. N. Kariuki, W. J. Khudhayer, T. Karabacak, and D. J. Myers, Glad Pt–Ni alloy nanorods for oxygen reduction reaction. *ACS Catal.,* **3** (12), 3123-3132 (2013).
29. T. Karabacak and T.-M. Lu, Enhanced step coverage by oblique angle physical vapor deposition. *J. Appl. Phys.,* **97** (12), 124504 (2005).
30. W. J. Khudhayer, N. Kariuki, D. J. Myers, A. U. Shaikh, and T. Karabacak, GLAD Cr nanorods coated with SAD Pt thin film for oxygen reduction reaction. *J. Electrochem. Soc.***, 159** (6), B729 (2012).
31. H. Cansizoglu, M. Cansizoglu, M. Yurukcu, W. Khudhayer, N. Kariuki, D. Myers, A. Shaikh, and T. Karabacak, In *SAD-GLAD core-shell nanorod arrays for fuel cell, photodetector, and solar cell electrode applications*, Nanoepitaxy: Materials and Devices VI, SPIE, 917411 (2014).
32. N. N. Kariuki, M. F. Cansizoglu, M. Begum, M. Yurukcu, F. M. Yurtsever, T. Karabacak, and D. J. Myers, SAD–GLAD Pt–Ni@ Ni nanorods as highly active oxygen reduction reaction electrocatalysts. *ACS Catal.,* **6** (6), 3478-3485 (2016).
33. B. Ergul, M. Begum, N. Kariuki, D. J. Myers, and T. Karabacak, Oxygen reduction reaction activity of platinum thin films with different densities. *ECS Trans.,* **80** (8), 847 (2017).
34. M. Demirkan, L. Trahey, and T. Karabacak, Low-density silicon thin films for lithium-ion battery anodes. *Thin Solid Films,* **2 600**, 126-130 (2016).
35. T. Ozkan, M. T. Demirkan, K. A. Walsh, T. Karabacak, and A. A. Polycarpou, Density modulated nanoporous tungsten thin films and their nanomechanical properties. *J. Mater. Res.,* **31** (14), 2011 (2016).
36. F. Keles, H. Cansizoglu, E. O. Badraddin, M. P. Brozak, F. Watanabe, and T. Karabacak, HIPS-GLAD core shell nanorod array photodetectors with enhanced photocurrent and reduced dark current. *Mater. Res. Express,* **3** (10), 105028 (2016).
37. F. Keles, H. Cansizoglu, M. Brozak, E. Badraddin, and T. Karabacak, Conformal core-shell nanostructured photodetectors with enhanced photoresponsivity by high pressure sputter deposition. *MRS Adv.,* **1** (28), 2045-2050 (2016).
38. M. Demirkan, L. Trahey, and T. Karabacak, Cycling performance of density modulated multilayer silicon thin film anodes in Li-ion batteries. *J. Power Sources,* **273**, 52-61 (2015).
39. H. Cansizoglu, M. F. Cansizoglu, and T. Karabacak, Effect of shell coating techniques on dynamic response of photoconductive core/shell nanorod arrays. *Adv. Mat. Interfaces,* **2** (16), 1500275 (2015).
40. H. Cansizoglu, M. Yurukcu, M. Cansizoglu, and T. Karabacak, Investigation of physical vapor deposition techniques of conformal shell coating for core/shell structures by Monte Carlo simulations. *Thin Solid Films, **583***, 122-128 (2015).
41. T. Karabacak, J. J. Senkevich, G.-C. Wang, and T.-M. Lu, Stress reduction in sputter deposited films using nanostructured compliant layers by high working-gas pressures. *J. Vac. Sci. Technol,* **23** (4), 986-990 (2005).

42. B. Ergul-Yilmaz, M. Begum, Z. Yang, M. L. Perry, K. L. More, N. Macauley, R. L. Borup, and T. Karabacak, Oxygen Reduction Reaction Activity of Nanocolumnar Platinum Thin Films by High Pressure Sputtering. *J. Electrochem. Soc.,* **167** (13), 134508 (2020).
43. B. Ergul-Yilmaz, Z. Yang, M. L. Perry, K. L. More, N. Macauley, R. L. Borup, and T. Karabacak, Microstructural Evolution and ORR Activity of Nanocolumnar Platinum Thin Films with Different Mass Loadings Grown by High Pressure Sputtering. *J. Electrochem. Soc.,* **167** (13), 134514 (2020).
44. M. Debe, A. Steinbach, G. Vernstrom, S. Hendricks, M. Kurkowski, R. Atanasoski, P. Kadera, D. Stevens, R. Sanderson, and E. Marvel, Extraordinary oxygen reduction activity of Pt3Ni7. *J. Electrochem. Soc.,* **158** (8), B910 (2011).
45. V. R. Stamenkovic, B. Fowler, B. S. Mun, G. Wang, P. N. Ross, C. A. Lucas, and N. M. Marković, Improved oxygen reduction activity on Pt3Ni (111) via increased surface site availability. *Science***, 315** (5811), 493-497 (2007).
46. F. M. Yurtsever, M. Yurukcu, M. Begum, F. Watanabe, and T. Karabacak, Stacked and Core–Shell Pt: Ni/WC Nanorod Array Electrocatalyst for Enhanced Oxygen Reduction Reaction in Polymer Electrolyte Membrane Fuel Cells. *ACS Appl. Energy Mater.,* **1** (11), 6115-6122 (2018).
47. J. A. Thornton, High rate thick film growth. *Annu. Rev. Mater. Sci.,* **7** (1), 239-260 (1977).
48. J. A. Thornton, In *Structure-zone models of thin films*, Modeling of Optical Thin Films, *SPIE*, 95-105 (1988).
49. S. E. Temmel, E. Fabbri, D. Pergolesi, T. Lippert, and T. J. Schmidt, Investigating the role of strain toward the oxygen reduction activity on model thin film Pt catalysts. *ACS Catal.* **6** (11), 7566-7576 (2016).
50. T. Karabacak, A. Mallikarjunan, J. P. Singh, D. Ye, G.-C. Wang, and T.-M. Lu, β-phase tungsten nanorod formation by oblique-angle sputter deposition. *Appl. Phys. Lett.,* **83** (15), 3096-3098 (2003).
51. Y. Garsany, O. A. Baturina, K. E. Swider-Lyons, and S. S. Kocha, Experimental methods for quantifying the activity of platinum electrocatalysts for the oxygen reduction reaction. *Anal. Chem*., **82**, 15, 6321–6328 (2010).
52. K. R. Cooper, In situ PEM fuel cell electrochemical surface area and catalyst utilization measurement. *Fuel Cell Magazine,* **9**, 28 (2009).
53. K. Mayrhofer, B. Blizanac, M. Arenz, V. Stamenkovic, P. Ross, and N. Markovic, The impact of geometric and surface electronic properties of Pt-catalysts on the particle size effect in electrocatalysis. *J. Phys. Chem. B,* **109** (30), 14433-14440 (2005).
54. D. Van der Vliet, C. Wang, M. Debe, R. Atanasoski, N. M. Markovic, and V. R. Stamenkovic, Platinum-alloy nanostructured thin film catalysts for the oxygen reduction reaction. *Electrochim. Acta* **56** (24), 8695-8699 (2011).
55. P. Mani, R. Srivastava, and P. Strasser, Dealloyed Pt− Cu core− shell nanoparticle electrocatalysts for use in PEM fuel cell cathodes. *J. Phys. Chem. C,* **112** (7), 2770-2778 (2008).
56. J. Snyder, I. McCue, K. Livi, and J. Erlebacher, Structure/processing/properties relationships in nanoporous nanoparticles as applied to catalysis of the cathodic oxygen reduction reaction. *J. Am. Chem. Soc.,* **134** (20), 8633-8645 (2012).

57. W. J. Khudhayer, N. N. Kariuki, X. Wang, D. J. Myers, A. U. Shaikh, and T. Karabacak, Oxygen reduction reaction electrocatalytic activity of glancing angle deposited platinum nanorod arrays. *J. Electrochem. Soc.,* **158** (8), B1029 (2011).
58. S. S. Kocha, K. Shinozaki, J. W. Zack, D. J. Myers, N. N. Kariuki, T. Nowicki, V. Stamenkovic, Y. Kang, D. Li, and D. Papageorgopoulos, Best practices and testing protocols for benchmarking ORR activities of fuel cell electrocatalysts using rotating disk electrode. *Electrocatalysis*, **8** (4), 366-374 (2017)**.**

Tables

Pt:Ni ratio	Pt loading ($\mu g_{Pt}/cm^2$)	2θ (°)	d spacing (Å)	grain size (nm)	strain (%)	Ni at.%		
						EDS	*XRD*	*QCM*
3:1	20	40.73	2.21	6	2		22	27
	48	40.51	2.23	6	1	27	17	
	94	40.56	2.22	8	2		19	
1:1	20	41.32	2.18	6	3		36	51
	48	41.36	2.18	6	3	45	36	
	94	41.43	2.18	9	4		38	
1:3	20	42.75	2.11	4	6		66	75
	48	42.65	2.12	7	6	75	64	
	94	42.94	2.11	7	7		70	

Table 1. *Comparison of composition of Ni, d-spacing, 2θ position, strain, and grain size of nanocolumnar Pt:Ni-TFs of 3:1, 1:1, and 1:3 compositions with Pt mass loadings of 20, 48, and 94 μg/cm² deposited on MPL-like surfaces at 3.93x10⁻² mbar sputtering pressure.*

	Pt:Ni (3:1)						Pt:Ni (1:1)						Pt:Ni (1:3)					
Pt loading ($\mu g_{Pt}/cm^2$)	ECSA (m^2/g)		SA ($\mu A/cm^2$)		MA (A/mg)		ECSA (m^2/g)		SA ($\mu A/cm^2$)		MA (A/mg)		ECSA (m^2/g)		SA ($\mu A/cm^2$)		MA (A/mg)	
	pre	*post*	*pre*	*post*	*pre*	*post*	*pre*	*post*	*pre*	*post*	*pre*	*post*	*pre*	*post*	*pre*	*post*	*pre*	*post*
~20	35	26	586	583	0.20	0.15	34	25	1095	794	0.37	0.20	42	33	1196	809	0.51	0.27

~48	28	22	710	706	0.20	0.16	27	21	1183	793	0.33	0.16	38	26	1781	855	0.66	0.22
~94	22	15	955	799	0.21	0.12	26	20	1654	890	0.43	0.17	34	21	1842	921	0.64	0.19

Table 2. *Electrochemical activity of nanocolumnar Pt:Ni-TFs of 3:1, 1:1, and 1:3 compositions with Pt mass loadings of 20, 48, and 94 μg/cm^2 deposited on MPL-like surfaces before and after 3,000 cycles of durability testing in 0.1 M $HClO_4$.*

Figures

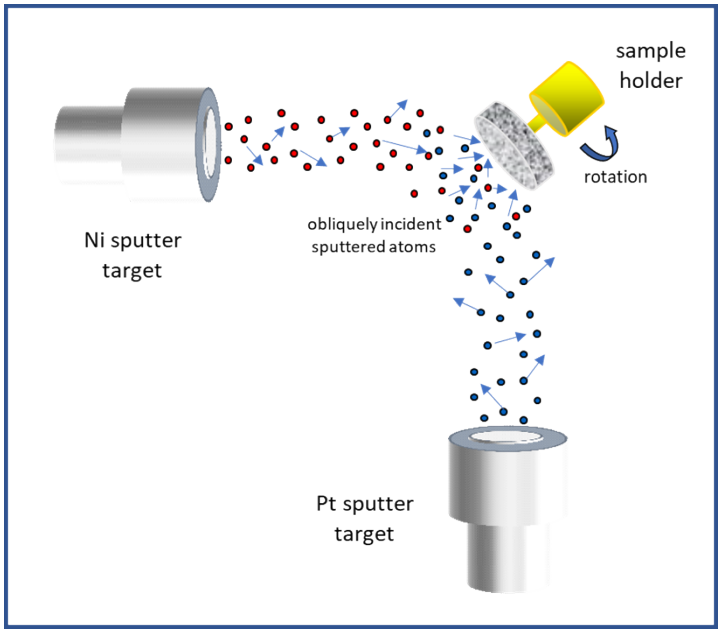

Figure 1. *Illustration of HIPS approach during Pt-Ni co-sputtering.*

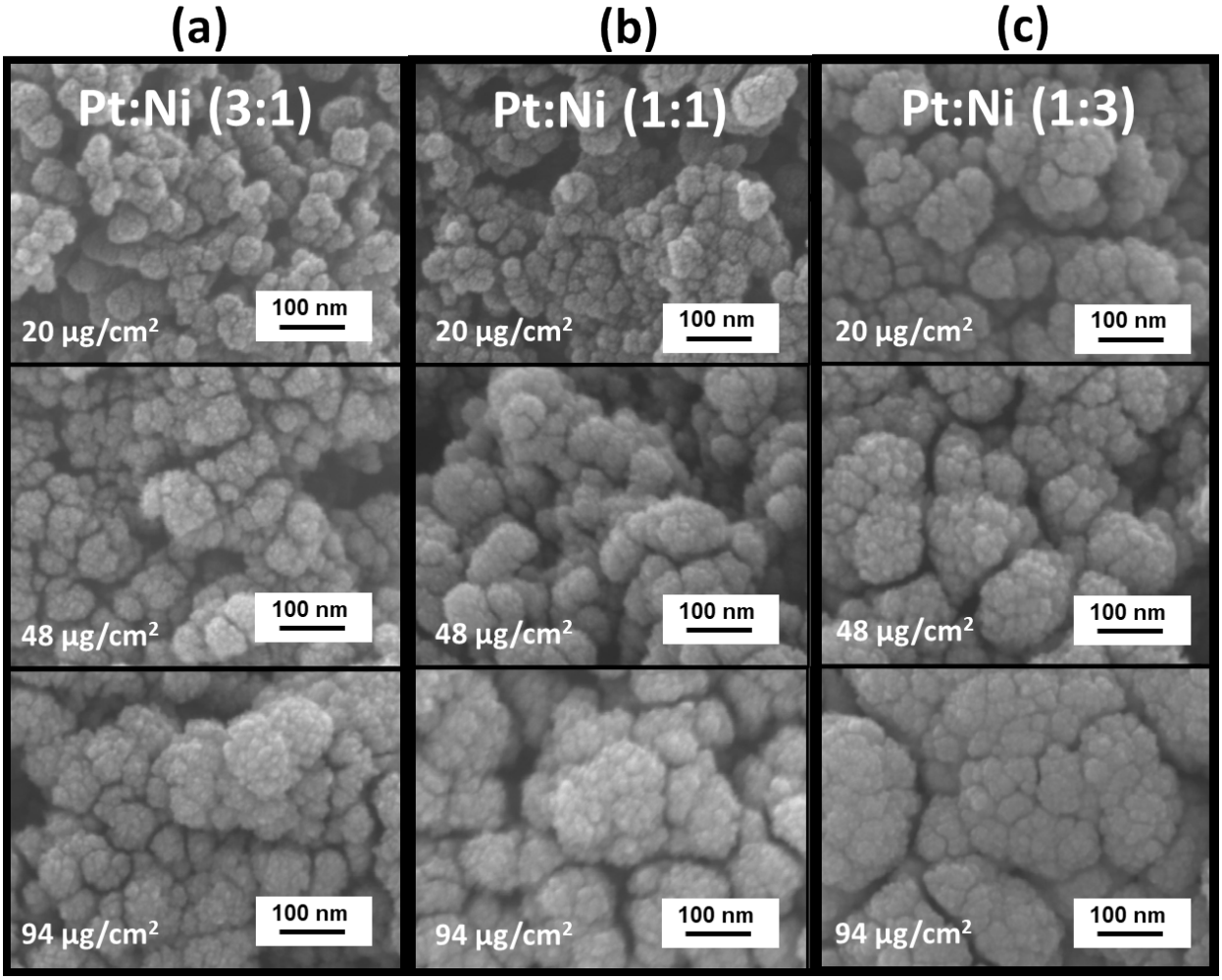

Figure 2. *Top-view SEM images of nanocolumnar Pt:Ni-TFs deposited on MPL-like surfaces at 3.93x10^{-2} mbar sputtering pressure with Pt mass loadings of ~20, 48, and 94 µg$_{Pt}$/cm^2 for a) (3:1), b) (1:1), and c) (1:3) atomic ratios.*

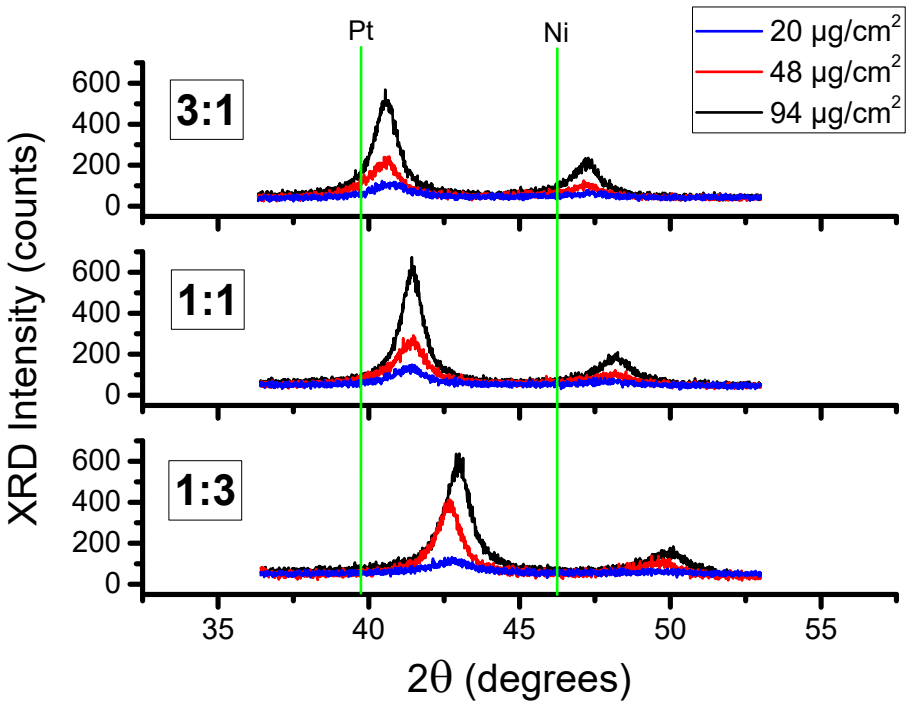

Figure 3. *XRD profiles of nanocolumnar Pt:Ni TFs with different Pt:Ni compositions with ~20, 48, and 94 $\mu g_{Pt}/cm^2$ mass loadings deposited on MPL-like surfaces at $3.93x10^{-2}$ mbar sputtering pressure. Green lines correspond to the elemental Pt(111) and Ni(111) peak positions.*

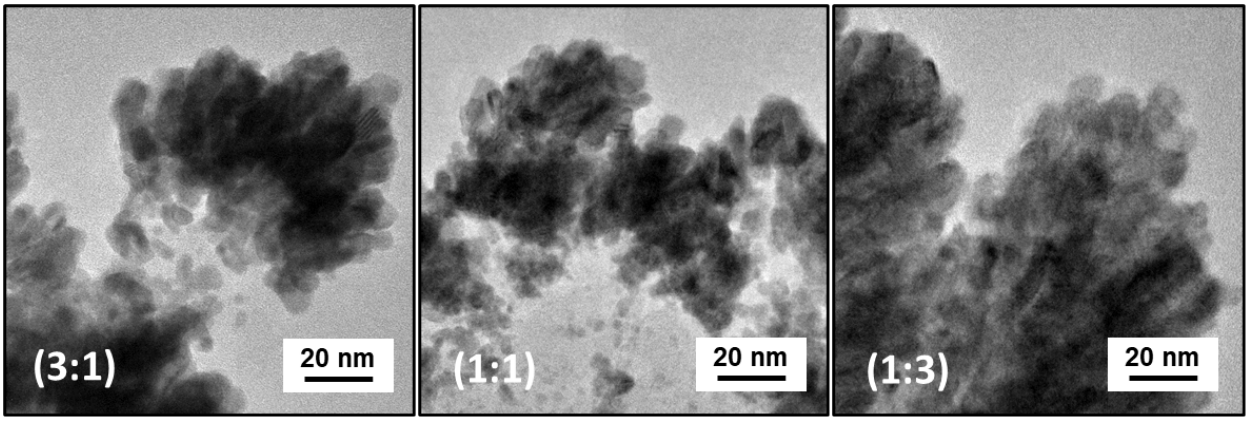

Figure 4. *TEM images of nanocolumnar Pt:Ni-TFs with different Pt:Ni compositions with ~48 $\mu g_{Pt}/cm^2$ deposited on MPLs at $3.93x10^{-2}$ mbar sputtering pressure.*

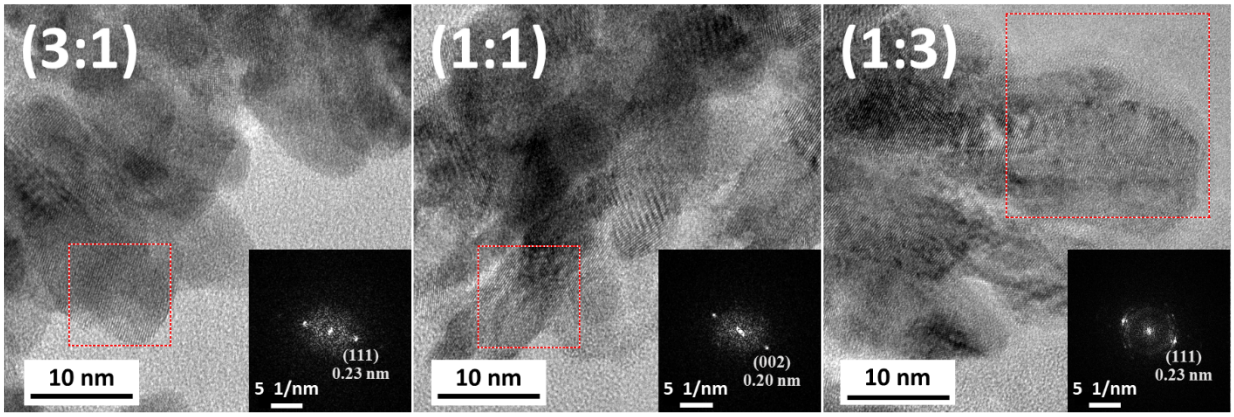

Figure 5. *HRTEM images and FFT patterns (inset) of Pt:Ni-TFs with different Pt:Ni compositions with ~48 $\mu g_{Pt}/cm^2$ deposited on MPLs at $3.93x10^{-2}$ mbar sputtering pressure.*

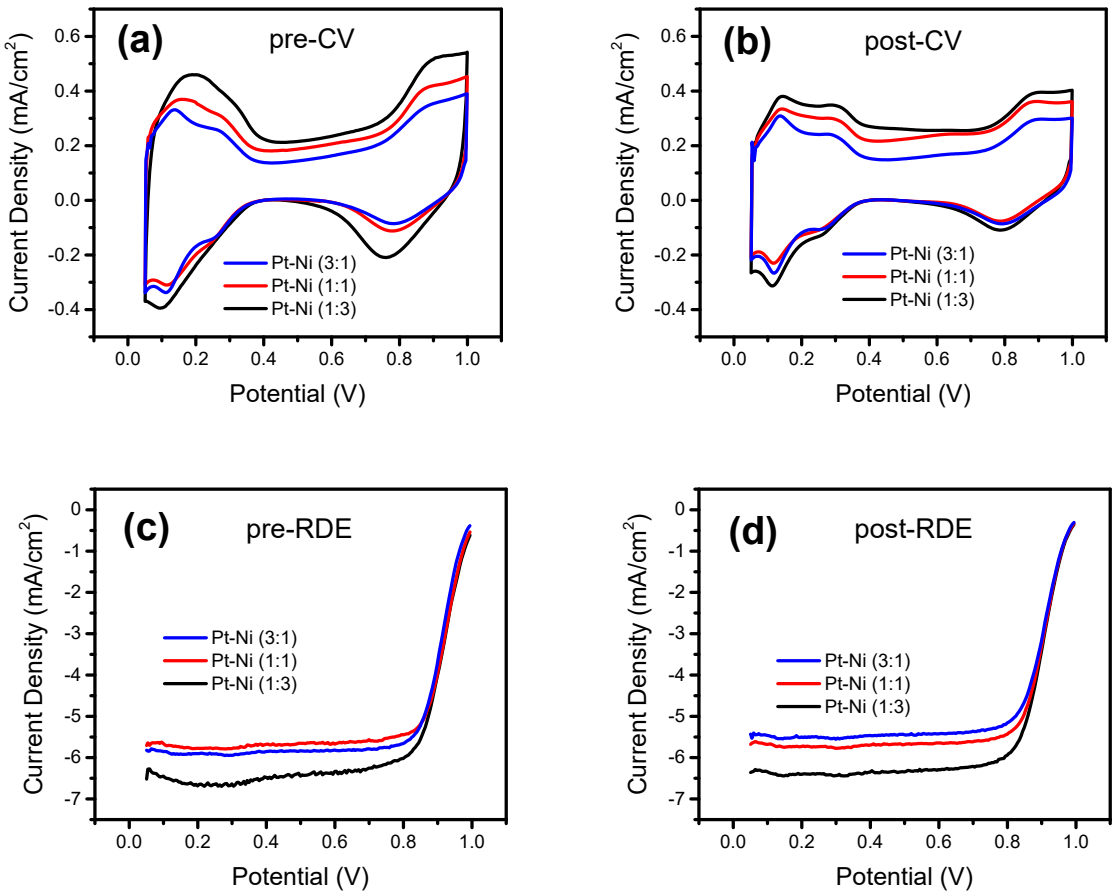

Figure 6. a) *CVs of nanocolumnar Pt:Ni-TFs with different ratios of ~48 $\mu g_{Pt}/cm^2$ deposited on MPL-like surfaces at $3.93x10^{-2}$ mbar sputtering pressure before (pre) and* ***b)*** *after (post) 3,000 cycles of durability cycling.* ***c)*** *ORR polarization curves of nanocolumnar Pt:Ni-TFs with different ratios of ~48 $\mu g_{Pt}/cm^2$ deposited on MPL-like surfaces at $3.93x10^{-2}$ mbar sputtering pressure before (pre) and* ***d)*** *after (post) 3,000 cycles of durability cycling. Scan rate was 20 mV/s and 1600 rpm rotation speed.*